ACSNANO

www.acsnano.org

ARTICLE

Beyond Volume Variation: Anisotropic and Protrusive Lithiation in Bismuth Nanowire

Yifei Yuan,[§] Wentao Yao,[§] Vitaliy Yurkiv,* Tongchao Liu, Boao Song, Farzad Mashayek, Reza Shahbazian-Yassar,* and Jun Lu*

Cite This: *ACS Nano* 2020, 14, 15669–15677

Read Online

ACCESS | Metrics & More | Article Recommendations | Supporting Information

ABSTRACT: **Materials storing energy *via* an alloying reaction are promising anode candidates in rechargeable lithium-ion batteries (LIBs) due to their much higher energy density than the current graphite anode. Until now, the volumetric expansion of such electrode particles during lithiation has been considered as solely responsible for cycling-induced structural failure. In this work, we report different structural failure mechanisms using single-crystalline bismuth nanowires as the alloying-based anode. The Li−Bi alloying process exhibits a two-step transition, that is, Bi−Li_1Bi and Li_1Bi−Li_3Bi. Interestingly, the Bi−Li_1Bi phase transition occurs not only in the bulk Bi nanowire but also on the particle surface showing its characteristic behavior. The bulk alloying kinetics favors a Bi-(012)-facilitated anisotropic lithiation, whose mechanism and energetics are further studied using the density functional theory calculations. More importantly, the protrusion of Li_1Bi nanograins as a result of anisotropic Li−Bi alloying is found to dominate the surface morphology of Bi particles. The growth kinetics of Li_1Bi protrusions is understood atomically with the identification of two different controlling mechanisms, that is, the dislocation-assisted strain relaxation at the Bi/Li_1Bi interface and the short-range migration of Bi supporting the off-Bi growth of Li_1Bi. As loosely rooted to the bulk substrate and easily peeled off and detached into the electrolyte, these nanoscale protrusions developed during battery cycling are believed to be an important factor responsible for the capacity decay of such alloying-based anodes at the electrode level.**

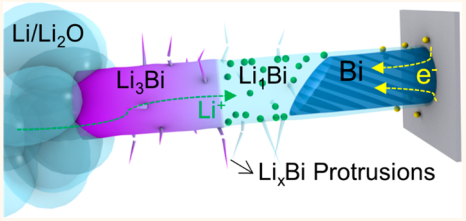

KEYWORDS: *in situ transmission electron microscopy, bismuth, lithium ion battery, protrusive alloying, density functional theory*

Materials storing Li^+ through alloying reactions, such as Si, Ge, Se, and Bi, are attracting growing research interest due to their high capacity and energy density compared to the commercialized intercalation-based graphitic anode in lithium-ion batteries (LIBs).[1,2] However, the high energy density of this type of anode materials comes at the expense of structural stability, as evidenced by the fast capacity decay upon cycling. The origin for such structural instability of alloying-based anode materials has been mostly, if not solely, explained by the severe volume change during the repetitive Li^+ insertion and extraction, either isotopically or anisotropically.[1,3,4] As a representative, Bi, whose theoretical volumetric capacity is as high as 3800 mAh·cm^{-3} with Li_3Bi as the final lithiated phase, has been widely studied as a promising anode candidate.[4−9] To understand the capacity decay mechanisms of Bi, various *in situ*/*ex situ* approaches have been applied, the results of which have led to the identification of cycling-induced volumetric variation as the cause of structural failure.[10−15] Yet, such analyses are generally at the electrode level and cannot provide the reaction kinetics on the single-particle level, not to mention any atomic details that are necessary to deduce potentially existing subtle mechanisms. With downsizing alloying-based electrode particles to nanoscale becoming a common strategy to improve energy storage performance, locally sensitive *in situ* characterization at high resolution is necessitated in order to further rationally design LIBs based on these anode chemistries.

Herein, we explored the (de)lithiation behaviors of single-crystalline Bi nanowires using *in situ* synchrotron X-ray diffraction (XRD) and *in situ* open-cell transmission electron microscopy (TEM) techniques. *In situ* XRD, by transmitting a high-intensity and high-energy X-ray beam through the interested electrode materials sealed in a routinely working coin cell, provides collective phase evolution information on the ensemble of electrode nanoparticles in the range of hundreds of microns. *In situ* TEM, by transmitting a normal electron beam through an interested electrode particle being simultaneously (dis)charged inside the vacuum pole-piece gap

Received: August 6, 2020
Accepted: October 26, 2020
Published: November 4, 2020

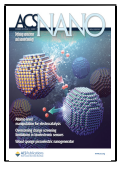

https://dx.doi.org/10.1021/acsnano.0c06597
ACS Nano 2020, 14, 15669−15677

of an electron microscope, is good at directly visualizing nanoscale and atomic-scale reaction kinetics of single particles. Therefore, the combination of these multiscale *in situ* techniques enables us to comprehensively understand the Li−Bi alloying mechanisms and to convincingly demonstrate the characteristic Li−Bi alloying kinetics different to the other alloying-based materials such as Si, Sn, Ge, *etc.* We confirmed the two-step lithiation mechanism of Bi featuring the Bi−Li_1Bi transition and Li_1Bi−Li_3Bi transition at both the electrode level and the single-particle level. In addition, the diffusion of Li^+ ions within single Bi nanowire features an energetically favorable pathway along Bi-(012) planes as understood by both experimental observation and the density functional theory (DFT) calculations. More importantly, the protrusive growth of alloyed phases on the surface of Bi nanowires is observed at the atomic level and is found to be controlled by either dislocation-mediated interfacial precipitation or short-range migration of Bi atoms at the particle surface. Seen to be loosely rooted to the Bi substrate, such protrusive nanograins should be at least partially responsible for the cycling instability of Bi as alloying-based anode materials and should thus call for future attention/effort to efficiently address the problem of structural failure in battery electrodes.

RESULTS AND DISCUSSION

Structure Analysis of As-Synthesized Bi Nanowires. The morphology and structure of the as-synthesized Bi nanowires are analyzed in Figure 1. It could be seen that the Bi nanowire has a diameter of ∼100 nm and its elemental composition is further confirmed by energy dispersive spectroscopy (EDS) to be pure crystalline Bi, as shown in the inset of Figure 1b as well as in Supporting Information Figure S1. The atomic structure of the same nanowire is demonstrated in Figure 1c. The atomic pattern agrees with the theoretical [001]-projection atomic model of Bi (rhombohedral phase [space group: *R*3*m* (166)]), based on which the growth direction of Bi nanowire is determined to be [100]. Figure 1d shows the atomic structure of a Bi nanowire along a different zone axis, Bi-[241], where the growth direction is also determined to be [100]. So it is reasonable to expect that the growth direction of Bi nanowires synthesized using the hydrothermal method in this work is [100].

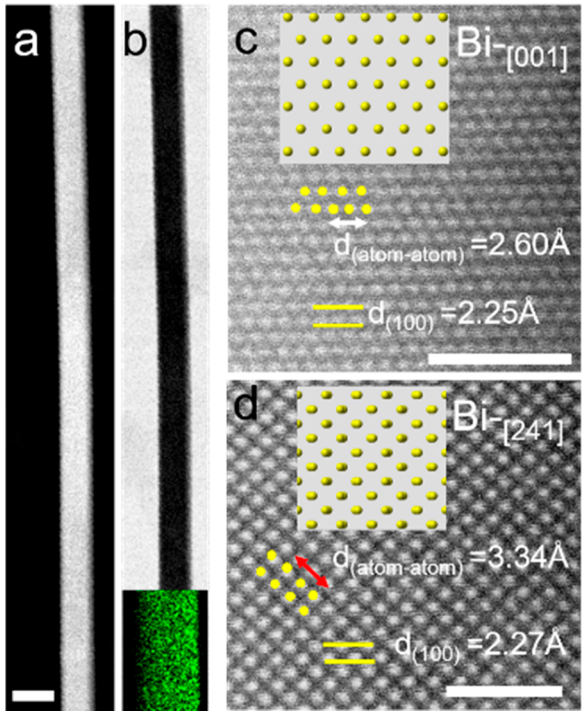

Figure 1. TEM analyses of Bi nanowires. (a, b) Low-magnification high-angle annular dark-field (HAADF) and bright field (BF) images of single Bi nanowire, respectively. Inset of (b) shows the elemental mapping of Bi using EDS. (c, d) HAADF atomic image of Bi nanowires viewed along two different zone axes, namely Bi-[001] and Bi-[241]. Insets show the corresponding atomic model of the theoretical Bi structure with the yellow spheres standing for Bi atoms. Scale bar in (a) is 100 nm. The scale bars in (c, d) are 2 nm.

Two-Step Li−Bi Alloying Mechanism. The (de)-lithiation reactions of Bi are first explored using a coin-cell-based configuration where Li metal foil is used as the anode and the laminated Bi electrode of interest is used as the cathode. The voltage profile as a function of (dis)charge capacity during the first cycle is shown in Figure 2a. During lithiation, the profile features two long plateaus with the first one at ∼0.8 V and the second one at ∼0.7 V, indicating that the lithiation of Bi is characteristic of two two-phase reactions. It is also interesting to note that while the first lithiation plateau contributes a capacity of ∼200 mAh/g, the second plateau almost doubles its contribution to ∼400 mAh/g. More importantly, these two two-phase reactions are largely reversible during the delithiation reaction, as evidenced by the two long plateaus appearing at ∼0.84 V and ∼0.87 V, respectively, with a similar 1:2 ratio regarding their specific delithiation capacity, as highlighted in the inset of the enlarged region of interest.

To further understand the two-phase reactions observed during the first lithiation−delithiation cycle, *in situ* synchrotron XRD is used to track the electrode-level phase evolution using laminated Bi nanowires inside the same coin cell being cycled. Figure 2b shows the phase analyses of the Bi nanowire electrode at various (de)lithiation states numbered from states 1 to 14, which correspond to the 14 characteristic states highlighted in the voltage profile in Figure 2a. The XRD of state 1 demonstrates the pure Bi phase in the electrode prior to lithiation. Immediately after the lithiation initiation at state 2, the starting point of the first lithiation plateau, peaks corresponding to the phase of Li_1Bi appear and gradually become intensified from states 2 to 7. The original peaks of Bi, on the other hand, gradually fade away and totally disappear at state 7, indicating the existence of a two-phase lithiation process featuring the following reaction for this plateau:

$$Bi + Li^+ + e^- = Li_1Bi \quad (1)$$

For the second lithiation plateau, XRD patterns of the states 6−10 demonstrate the gradual decrease of the intensity of the Li_1Bi peaks and the gradual increase of the intensity of a new phase indexed to be Li_3Bi. The two-phase lithiation process for this plateau is deduced as

$$Li_1Bi + 2Li^+ + 2e^- = Li_3Bi \quad (2)$$

The respective storage of 1 Li^+ ions and 2 Li^+ ions in eqs 1 and 2 agrees with the 1:2 ratio of the capacity contributions from the two plateaus as discussed above, which further confirms the accuracy of these two equations in describing the actual alloying behaviors of Li and Bi metals. Such a phase evolution

https://dx.doi.org/10.1021/acsnano.0c06597
ACS Nano 2020, 14, 15669−15677

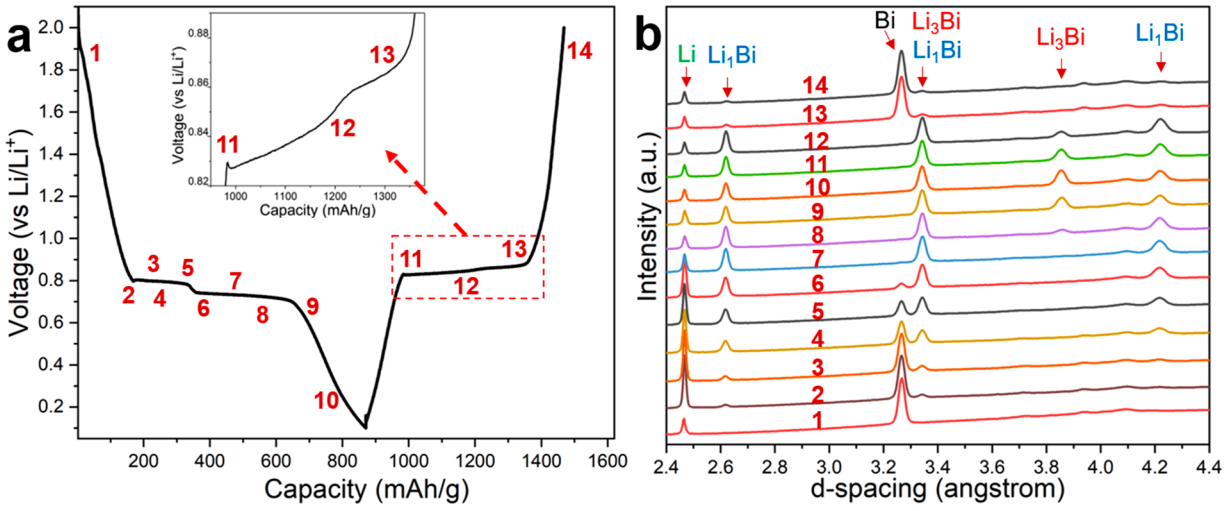

Figure 2. *In situ* synchrotron XRD analyses of Bi nanowires tested as laminated electrodes working inside a coin cell. (a) The voltage profile of the first discharge−charge cycle of a Li−Bi battery using Bi nanowires as the target electrode and Li metal as the counter electrode. Inset is the enlarged view of the plateau area during charge. A galvanostatic mode is used in the battery cycling with a constant current value of 40 mA/g. (b) Corresponding *in situ* synchrotron XRD patterns of the 14 data points highlighted in (a) at various states of (de)lithiation. XRD characteristic peaks characteristic of Li, Bi, Li_1Bi, and Li_3Bi phases are indicated.

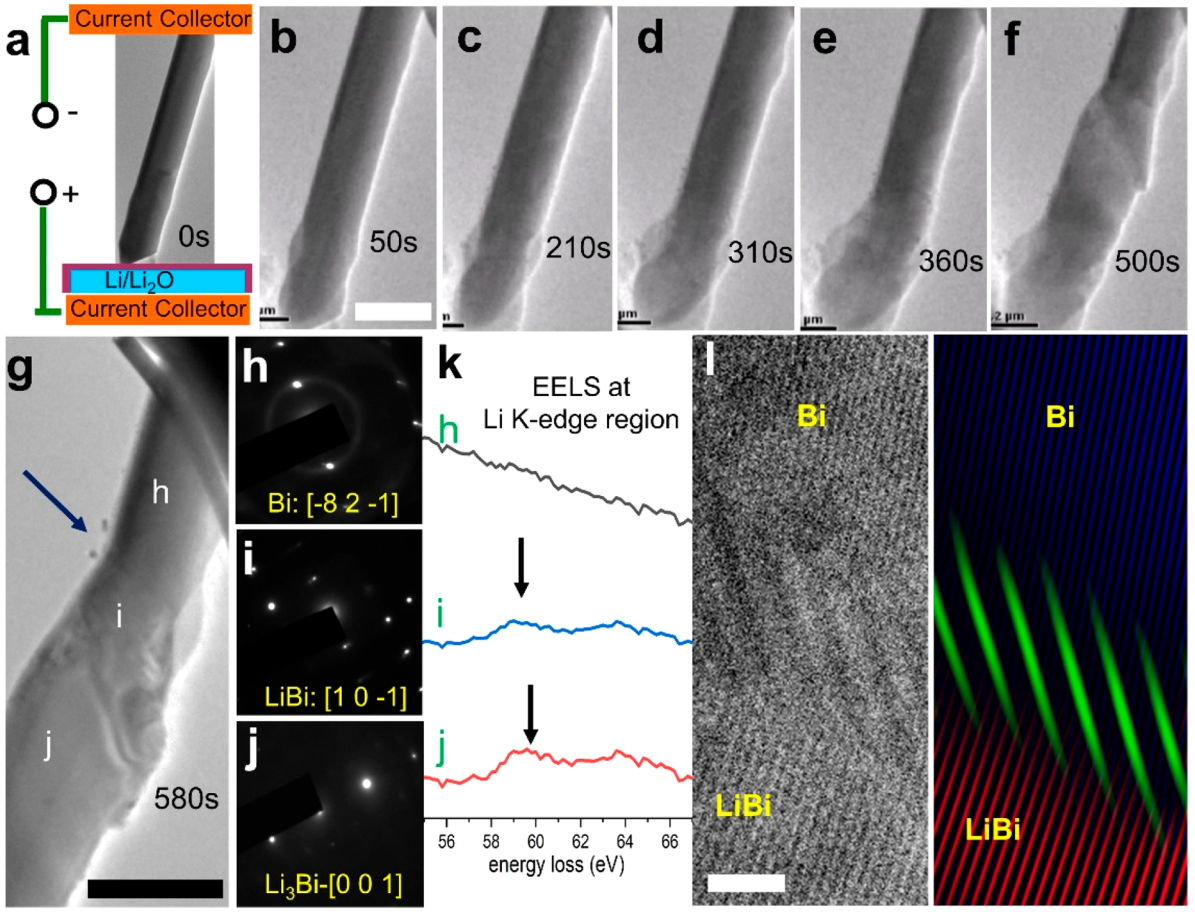

Figure 3. *In situ* TEM observation of the two-step Li−Bi alloying mechanism at the single-nanoparticle level. (a−g) Time-sequential TEM images showing the lithiation process in a single-crystalline Bi nanowire using Li/Li_2O as the counter electrode/electrolyte. (h−j) Selected area diffraction patterns for regions h−j marked in (g) exhibiting sharply different contrast and different degrees of lithiation. The corresponding phase of each region as well as their imaging zone axis are indexed in yellow text. (k) Electron energy loss spectroscopic analysis for regions h−j marked in (g) with the Li K-edge region zoomed in for qualitative comparison of Li content. (l) HAADF image and the corresponding IFFT. The Moire pattern is highlighted in green. Scale bars in (b−g) are 200 nm and in (l) is 2 nm.

https://dx.doi.org/10.1021/acsnano.0c06597
ACS Nano 2020, 14, 15669−15677

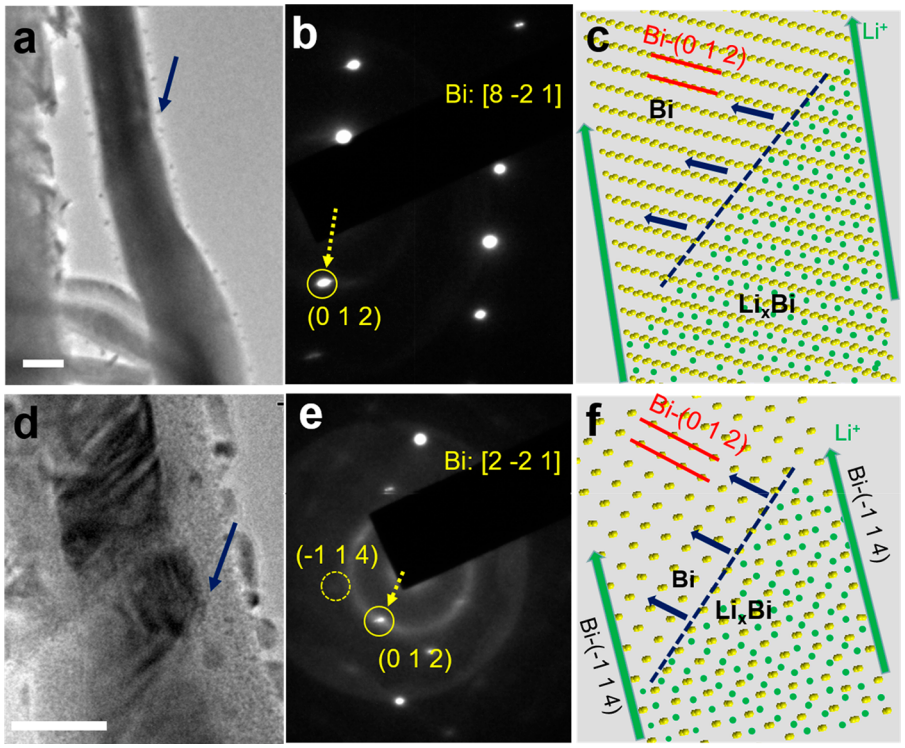

Figure 4. Understanding the (012)-facilitated Li^+ insertion in single-crystalline Bi nanowires. (a, d) TME images of partially lithiated single-crystalline Bi nanowires, where the blue arrows highlight the sloped phase Bi−Li_1Bi phase boundary. Scales bars are 50 nm. (b, e) SAED patterns for pristine Bi regions in (a, d), respectively. (c, f) Atomic modeling of the (012)-facilitated Li−Bi alloying mechanism.

can also be supported by the equilibrium phase diagram of Bi−Li, where Li_1Bi and Li_3Bi are shown to be the only two thermodynamically stable phases.[16]

The first delithiation plateau from states 11 to 12 is associated with the phase transition from Li_3Bi to Li_1Bi, as evidenced by the intensity decrease of Li_3Bi peaks and the intensity increase of Li_1Bi peaks. The second delithiation plateau from states 12 to 14 corresponds to the transition from Li_1Bi to metallic Bi, as evidenced by the disappearance of Li_1Bi peaks and the reoccurrence of Bi peaks. Therefore, the full delithiation process can be described by the following two reactions:

$$Li_3Bi = Li_1Bi + 2Li^+ + 2e^- \quad (3)$$

$$Li_1Bi = Bi + Li^+ + e^- \quad (4)$$

The ratio of the delithiation capacity contributed from these two reactions is about 2:1, further confirming the existence of such phase transitions during lithiation and delithiation. However, it is worth noting that there is an observable amount of residual Li_1Bi phase at the end of both the lithiation and delithiation, while the Li_3Bi phase is not observed after delithiation. This implies that the Bi−Li_1Bi phase transition might not be fully reversible and a portion of Li_1Bi is, for some reason, electrochemically deactivated during cycling and thus contributes to the capacity decay of the Bi anode (discharge capacity of 850 mAh/g *vs* charge capacity of 600 mAh/g based on Figure 2a). To identify the origin for the capacity decay, we further rely on *in situ* TEM analyses as later discussed.

Alloying-Induced Phase Boundary. In addition to the *in situ* synchrotron XRD analyses on the ensemble of numerous Bi nanowires, *in situ* TEM was utilized to explore the lithiation kinetics of a single Bi nanowire at both high temporal and high spatial resolution. Figure 3a demonstrates the experimental setup of *in situ* TEM of the lithiation of a single Bi nanowire using an open cell design, where Li/Li_2O is considered as the Li^+ source, while Bi is the working electrode. The full Li−Bi alloying process of the single Bi nanowire is given in Supporting Movie S1. As soon as the lithiation starts, a surface diffusion mechanism is first seen to dominate the initial lithiation process, as evidenced by the gradual expansion of the surface layer on Bi nanowire with an almost unchanged Bi core until the lithiation time goes to 210 s. The surface lithiation also results in precipitation of small nanograins with the grain size up to 10 nm (Figure 3g). After that, the lithiation of bulk Bi takes charge by exhibiting an obvious and drastic diameter expansion. Yet, the phase transition fronts are not obvious at the beginning, but they appear as sharp boundaries at ∼500 s by demonstrating two phase transition fronts. An enlarged view of the partially lithiated Bi nanowire at ∼580 s demonstrates three distinct regions separated by these two-phase transition fronts, which are named as regions h, i, and j. Their corresponding selected area electron diffraction (SAED) patterns are shown in Figure 3h−j, respectively. It is notable that the SAED patterns indicate the single-crystalline feature for regions h−j. Referring to the standard single-crystalline diffraction pattern of Bi, Li_1Bi, and Li_3Bi phases (Supporting Information Figure S1), they can be indexed to be along the zone axes of Bi-$[8\bar{2}1]$, Li_1Bi-$[10\bar{1}]$, and Li_3Bi-[001], respectively. The increase of Li content from region h to region i and to region j is further confirmed using electron energy loss spectroscopy, as shown in Figure 3k, where the increase of Li−K edge signal intensity is seen (the intensity of the zero-loss peak for each curve is normalized to the same value to facilitate the direct comparison). Therefore, one can conclude based on both the *in situ* XRD and *in situ* TEM

https://dx.doi.org/10.1021/acsnano.0c06597
ACS Nano 2020, 14, 15669−15677

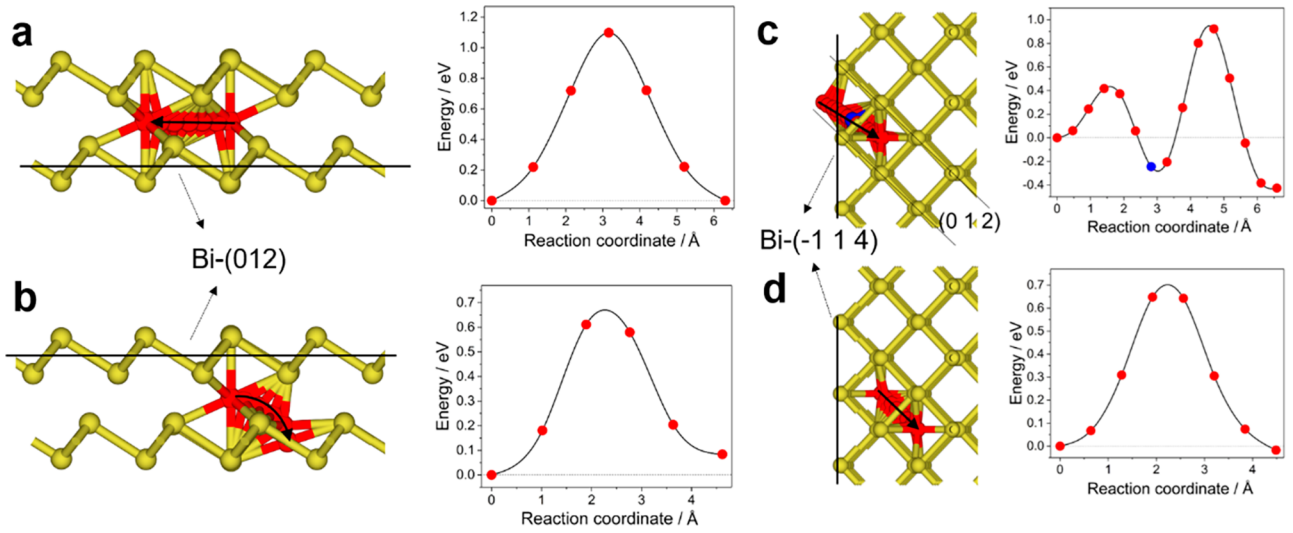

Figure 5. (a) The Li hopping between two equivalent octahedral sites (3*b*) and the corresponding migration barrier calculated at dilute Li concentration. (b) The Li hopping between a full octahedral (3*b*) position and a suppressed (3*a*) position within the Bi-(012) planes and the corresponding migration barrier calculated at dilute Li concentration. (c) The Li migration and calculated energy barriers for Bi-(012)-preferred Li insertion from the Bi-($\bar{1}$14) surface (adsorbate) to the subsurface position at dilute Li concentrations. (d) The Li migration and calculated energy barriers for further Li insertion from the subsurface position into Bi bulk (3*b* site) along Bi-(012).

results that the Li−Bi alloying process features a multistep lithiation mechanism at both the electrode level and single-nanoparticle level.

Note that multistep lithiation mechanisms have also been identified in single-crystalline nanoparticles of alloying-based materials such as Si, Sn, and Ge, where either polycrystalline or amorphous lithiated phases converted from an originally single-crystalline particle are reported.[17−20] The drastic structural change subjects crystalline anode materials to the generation of grain boundaries, particle pulverization, and excessive electrolyte consumption, which could lead to gradual fracturing of electrode materials as well as loss of cycling capacity. A significant characteristic of Bi alloying process compared to that of Si, Sn and Ge lies in its single-crystalline property of lithiated phases (Li_1Bi and Li_3Bi) within the single Bi nanowire, as confirmed in Figure 3i,j, which is expected to significantly alleviate the particle pulverization upon cycling. In addition, the Li/Li_1Bi two-phase boundary is further zoomed in with more details revealed in Figure 3l. Interestingly, a Moire pattern is observed (green color in the right panel), indicating that the Bi/Li_1Bi two-phase boundary is not vertical to the axis of the Bi nanowire and exhibits a certain crystallographic orientation related to the Bi substrate.

To further explore such a crystallographic feature, two partially lithiated Bi nanowires with the corresponding SAED patterns of unlithiated Bi are shown in Figure 4. Similar to the sloped Bi/Li_1Bi front observed in Figure 3, these two partially lithiated Bi nanowires also exhibit a sloped Bi/Li_1Bi front, as highlighted by blow arrows in Figure 4a,d. Referring to the diffraction spots existing in these two zone axes of Bi (Bi-[8$\bar{2}$1]- and Bi-[2$\bar{2}$1]), it is notable that both sets of patterns have the Bi-(012) diffraction (highlighted in solid yellow circle). More importantly, in the two SAEDs taken using an electron microscope with corrected magnetic rotation angle, the Bi-(012) plane indicated by the dashed yellow arrows is roughly vertical to the Bi/Li_1Bi phase boundary, implying the critical role of Bi-(012) in facilitating the initial lithiation behavior in Bi nanowires. Therefore, we propose the existence of Bi-(012)-facilitated Li^+ insertion kinetics during the Li−Bi alloying process, which is illustrated using atomic models under Bi-[8$\bar{2}$1] and Bi-[2$\bar{2}$1] projections in Figure 4c,f, respectively. Following the preceding surface diffusion (green arrows), Li^+ prefers to insert into the bulk Bi along the Bi-(012) interlayer spacing as the energy-favorable pathway (blue arrows). Under the synergistic influence of applied bias, the Bi/Li_1Bi phase boundary thus migrates along a characteristic direction, as indicated by the blue arrows in Figure 4c,f, causing the observable imaging contrast as shown in Figure 4a,d.

Alloying-Phase Boundaries Understood by DFT. We further carried out DFT-based calculations to understand why the (012)-facilitated Li^+ insertion in crystalline Bi and the fast surface lithiation could be experimentally observed. The favorable pathways for Li atom diffusion in the bulk of Bi as well as the insertion path from the most stable Bi surface into the bulk of Bi were studied. Figure 5a,b shows two possible Li diffusion paths in the bulk structure of Bi. The Li atom in the bulk Bi configuration can be present at two distinguished locations: the first location is an 8-fold (the full octahedral site) coordinated location between two neighboring Bi layers (3*b* in Wyckoff classification), and the second location of Li inside the Bi corresponds to the suppressed 8-fold configuration (3*a* in Wyckoff classification). More information about the Li location inside the Bi bulk structure is provided in Figure S2. Correspondingly, we studied two Li diffusion paths: one from the full octahedral site to the neighboring full octahedral site (Figure 5a), and the other one from the full octahedral site to the suppressed octahedral configuration (Figure 5b). The result shows that the energy barrier of Li^+ diffusing *via* direct 3*b*-to-3*b* pathway is about 1.1 eV, while this value is much smaller (~0.6 eV) *via* the 3*b*-to-3*a* pathway. This suggests that Li diffusion inside the Bi bulk structure probably proceeds through a hopping mechanism between 3*b* and 3*a* sites.

Next, an investigation of the Li diffusion pathways from surface into bulk was performed. We used the Bi-($\bar{1}$14) surface as an example since its diffraction spot has been experimentally identified in Figure 4e,f (dashed yellow circle). In order to evaluate the most stable surface adsorbate configuration, the Li

https://dx.doi.org/10.1021/acsnano.0c06597
ACS Nano 2020, 14, 15669−15677

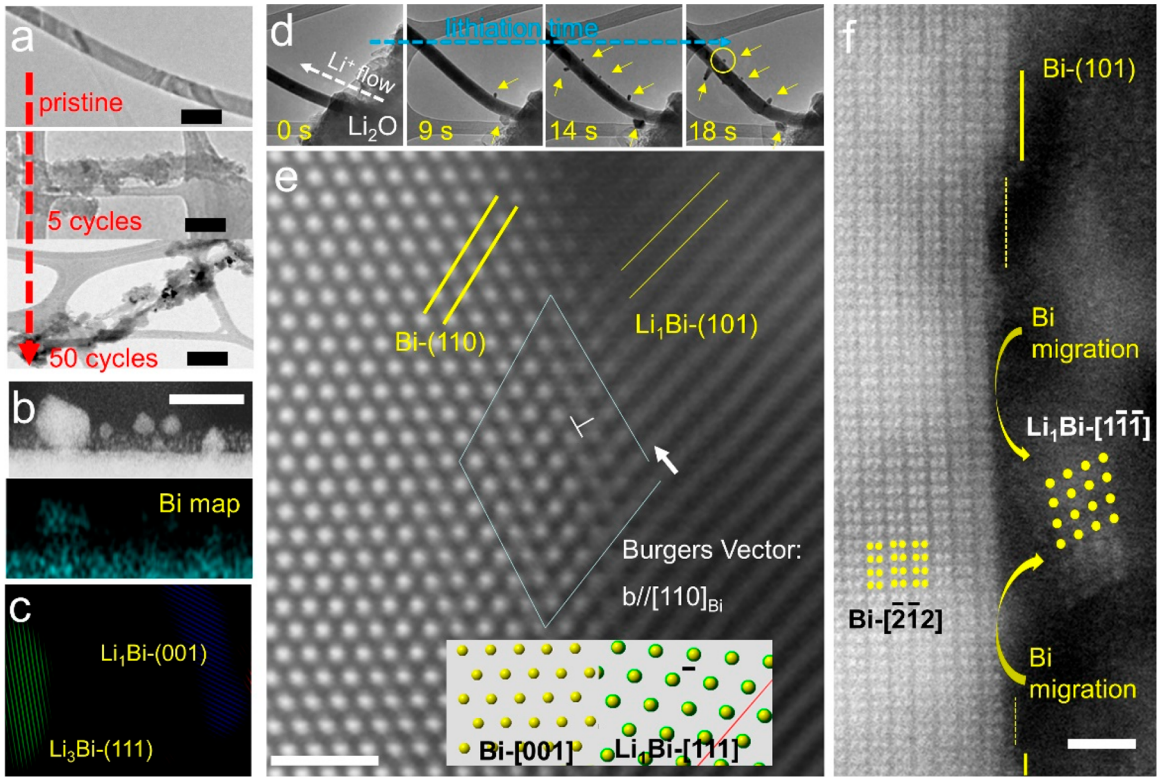

Figure 6. Atomic mechanism of the protrusive surface Li−Bi alloying process. (a) *Ex situ* TEM analyses showing the gradual fracturing and pulverization of Bi nanowires after 5 and 50 battery cycles. Scale bars are 200 nm. (b) The enlarged HAADF image of the surface precipitation as well as the EDS elemental mapping of Bi signal. The scale bar is 10 nm. (c) IFFT of the precipitated particles showing mixed Li_1Bi and Li_3Bi phases. (d) Time-sequential TEM images showing the protrusive growth of Li−Bi alloying precipitations (yellow arrows) on the Bi surface as a result of surface lithiation. (e) Atomic HAADF image of the interface between Bi substrate and one Li_1Bi protrusion during surface lithiation. Inset shows the atomic models of Bi-[001] and Li_1Bi-[$\bar{1}$11] projections that match the experimental observation. An edge dislocation at the interface region is identified. (f) Atomic HAADF image along Bi-[$\bar{2}\bar{1}2$] projection showing the consumption of one Bi-(101) atomic layer on the surface accompanied by the precipitation of one Li_1Bi nanograin imaged under its [$\bar{1}\bar{1}\bar{1}$] zone axis. Curved yellow arrows indicate the possible Bi atomic migration pathways on the surface. Scale bars in (e, f) are 1 nm.

binding energies on the Bi-($\bar{1}$14) surface were calculated. Figure S3 shows two Li adsorption possibilities on the surface of Bi, the top (left) and the bridge (right) configurations. It was found that the bridge site with the binding energy of −331.07 eV is more stable than the top one with the binding energy −330.23 eV. In our calculations, the binding energy was defined as the difference between the energy of the Li-adsorbed Bi-($\bar{1}$14) surface and the sum of the energies of a single Li atom and the Bi-($\bar{1}$14) surface. In the bridge configuration, Li resides equidistant between two Bi atoms with a Li−Bi bond length of 2.7 Å. Accordingly, we studied how the bridge-adsorbed Li penetrates into the bulk of Bi occupying the most probable and stable 3*b* position. Figure 5c shows the structure and potential energy for Bi-(012)-preferred Li diffusion into a subsurface location, whereas Figure 5d depicts further Li insertion into the bulk of Bi leading to 3*b* configuration. As demonstrated above, the stable site for Li insertion is the octahedral location where Li coordinates with 8 Bi atoms of bulk configuration. In the first step, surface Li diffuses into the subsurface location corresponding to the octahedral configuration. However, due to the Bi-($\bar{1}$14) subsurface structure, one bond is missing for a full 3*b* coordination, and this structure is thus slightly less stable than the Li−Bi bulk configuration. A local minimum in the global diffusion path to subsurface position was observed corresponding to the bridge bonding between the Li atom and the two Bi atoms of the second layer. There is an activation barrier for this intermediate configuration equal to 0.4 eV. Such a favorable position in the valley slightly below the uppermost surface layer is consistent with the other similar systems such as Li−Si.[21,22] We believe this energetically favorable subsurface position significantly facilitates the fast Li^+ insertion along the surface of Bi nanowires, which can account for the experimentally observed fast Li^+ diffusion along the surface region of Bi as discussed in Figure 3. The final subsurface configuration is more stable but is accompanied by a barrier of 0.65 eV. The migration path from the subsurface to the bulk 3*b* site has a barrier of 0.7 eV but is slightly more favorable than the subsurface location.

We have also calculated Li diffusion inside Li_1Bi and Li_3Bi phases (Figure S4). Much lower activation barriers for Li diffusion in these two phases are found compared to the pure Bi phase. Between Li_1Bi and Li_3Bi phases, the Li diffusion inside Li_3Bi is faster, occurring with a negligible barrier. This observation supports the experimentally observed phenomena of accelerated lithiation of Li_1Bi and Li_3Bi.

Protrusive Li−Bi Alloying on the Particle Surface. Figure S5 demonstrates the voltage profiles of the Li/Bi coin cell tested during the first 10 cycles and the 40th cycle, where the two-step alloying reactions of Bi−Li_1Bi and Li_1Bi−Li_3Bi appear during the first few cycles but decay fast upon cycling. Specifically, the cycling performance of Bi nanowires is severely

https://dx.doi.org/10.1021/acsnano.0c06597
ACS Nano 2020, 14, 15669−15677

degraded from an initial discharge capacity of 650 mAh/g to 100 mAh/g at the 10th discharge and to 60 mAh/g at the 40th discharge. Here, to further explore the intrinsic structural origins for the inferior performance of Bi, *ex situ* TEM analysis in Figure 6a reveals the severe structural damage of Bi nanowires during battery cycling, where the particle pulverization can be clearly seen after only 50 cycles. While the single-crystalline property of alloyed phases (Li_1Bi and Li_3Bi without intragrain boundary, as shown in Figure 3) in the bulk Bi is expected to effectively suppress particle pulverization, the observed structural degradation of cycled Bi should thus be caused by factor(s) other than the bulk lithiation kinetics.

As shown in Figures 3 and 4, another noticeable characteristic of Li−Bi alloying reaction is the protrusion of small nanograins on the surface of Bi nanowire, in addition to the two-step lithiation phenomenon in the bulk Bi. It is worth mentioning that other alloying-based anode materials, such as Si,[23] Ge,[24] Sn,[17] and Se,[25] although experiencing a similar volumetric variation upon battery cycling, have not been reported to exhibit any secondary particle protrusion on the surface. Figure 6b is the zoomed in scanning transmission electron microscopy-high-angle annular dark-field (STEM-HAADF) image capturing the surface precipitation on the surface of one lithiated Bi nanowire, where smaller nanograins with sizes of 2−10 nm are observed and confirmed to be Bi-rich. Combining the inverse fast Fourier transform (IFFT) analysis in Figure 6c, it can be concluded that these nanograins are a mixture of Li_1Bi and Li_3Bi phases which, instead of being uniformly distributed within the Bi substrate, protrude out of the substrate and become weakly bonded to bulk Bi. Such a protrusive growth of lithiated Bi phases during lithiation is further captured by *in situ* TEM, as shown in Figure 6d, where the continuous growth of protrusions, in a non-negligible amount, is clearly observed and highlighted in yellow arrows. It is also noticeable that these protrusions are loosely rooted to the inner bulk Bi substrate, which could be easily peeled off and detached into the electrolyte during harsh cycling conditions and lose their electrochemical activity, accounting for the observable presence of the Li_1B phase at the end of lithiation (Figure 2b, state 10) and the cycling-induced capacity decay as observed in Figure S5.

A closer look at Figure 6e reveals the atomic structure at the interface between the bulk Bi and one Li_1Bi nanograin protrusion, which exhibits a semicoherent boundary shared by Bi-(110) as the substrate and protrusive Li_1Bi-(101). Because of the relatively large lattice mismatch (~15%) between these two planes, edge dislocation is generated at the boundary region to alleviate the strain. Therefore, one mechanism accounting for the surface lithiation mechanism of Bi can be described as the dislocation-assisted strain relaxation and consequent protrusive growth of Li_1Bi nanograins, which is similar to the mechanism reported in lattice-mismatched heteroepitaxial film growth.[26] The driving force for the out-flowing of Bi atoms from the substrate could be ascribed to the non-negligible compressive stress generated during lithiation, similar to the case of other metals with a low melting point, such as Sn applied in electronic systems and batteries.[27−29] In addition to the dislocation-assisted protrusion, Figure 6f also demonstrates another mechanism for protrusive Li_1Bi growth on the surface of bulk Bi nanowire. It is notable in the surface regions adjacent to the protrusions that the outmost surface layer (Bi-(101)) of Bi atoms is depleted, as highlighted by the yellow dashed lines. Such Li_1Bi protrusions neighboring the depletion of Bi surface atoms indicate that the surface alloying reaction is at the expense of the surface Bi atoms *via* a short-range surface migration mechanism, as indicated by the yellow arrows. This surface migration mechanism results in off-substrate growth of the alloying phases, which is apparently different from the dislocation-assisted protrusion mechanism that still maintains the substrate-protrusion connection.

Overall, these two mechanisms observed here should account for the surface protrusion behaviors of alloyed phases, which weaken the bonding between Bi substrate and surface precipitates and ultimately lead to particle pulverization and capacity decay upon cycling. Previous studies have reported the positive effect of electrolyte selection and the use of carbon substrates on performance enhancement of Bi-based electrodes,[30,31] which provide feasible strategies to address the inferior cycling performance of Bi electrodes. It is therefore quite interesting to understand the role of such strategies in affecting the lithiation kinetics of Bi electrodes in the future. Figure 7 summarizes the lithiation kinetics of a Bi nanowire as discussed above.

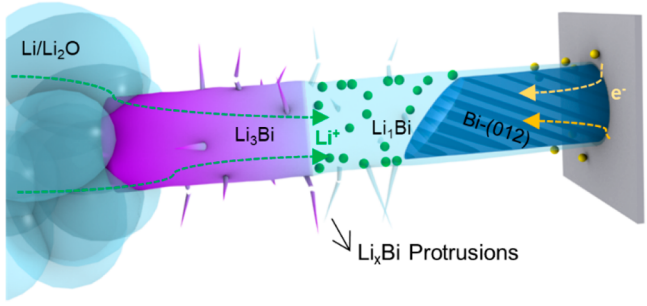

Figure 7. Schematic of the lithiation kinetics of a single Bi nanowire as observed in this work.

CONCLUSIONS

In short, the lithiation kinetics of single-crystalline Bi nanowires are demonstrated in real time and at high spatial resolution. A two-step Li−Bi alloying mechanism featuring a phase pathway of Bi−Li_1Bi−Li_3Bi is confirmed at both the electrode level and single-nanoparticle level. Li^+ diffusion into Bi exhibits Bi-(012)-facilitated kinetics, which is further understood *via* DFT. Surface protrusion of much smaller lithiated nanograins is identified, which exhibits a protrusive growth fashion and proceeds *via* two mechanisms: the dislocation-assisted strain relaxation and the short-range migration of Bi atoms on the surface. These protrusive nanograins are weakly bonded to the substrate and can continuously consume the bulk Bi particles upon cycling, which should thus be responsible for the cycling-induced structural failure and capacity decay of the electrodes. Our findings reveal characteristic lithiation kinetics in Bi materials and discover structural origins accounting for the structural degradation of alloying-based anode materials. Strategies like surface engineering are expected to be necessary and useful to address these concerns and to further improve the energy storage performance of such alloying-based materials.

METHODS

Material Synthesis. Bismuth nanowire was synthesized based on the reduction of sodium bismuthate dihydrate. In short, 0.1329 g of

https://dx.doi.org/10.1021/acsnano.0c06597
ACS Nano 2020, 14, 15669−15677

$NaBiO_3 \cdot 2H_2O$ and 0.1664 g of PVP (wt = 40,000) were dissolved in 35 mL of ethylene glycol under constant stirring. The mixture was bubbled with pure Ar gas for 30 min to avoid bismuth oxidation. The obtained solution was transferred to a 100 mL Teflon-lined stainless-steel autoclave and then heated at 180 °C for 24 h. The product was collected through vacuum filtration and then washed with ethanol three times. Finally, the Bi nanowire was dried at 50 °C for 1 h under vacuum.

TEM Characterization. *Ex situ* TEM analyses were done using a JEOL 3010 TEM equipped with a 300 kV electron gun (LaB_6). *In situ* TEM and atomic imaging were carried out using a probe-corrected STEM (JEOL-ARM200, cold-field emission gun) operated at 200 kV. To construct the battery inside the TEM chamber, a nanofactory biasing holder with two dangling metallic rods facing each other was used. For material loading, one rod was manipulated to gently scratch the surface of lithium metal, while the other one was dipped into a sonicated solution containing well-dispersed Bi nanowires and then lifted out. The holder with two rods, respectively, loaded with Li metal and Bi nanowires was quickly inserted into the microscope with an estimated air-exposure time of about 30 s. As a result, thin layers of Li_2O could form on the surface of Li metal and act as the solid-state electrolyte between Li and Bi electrodes. After the two skillfully loaded rods were connected to each other *via* their tips inside the microscope, a proper overpotential was applied to trigger the Li^+ insertion into Bi.

Electrochemical Test. Bi electrode on Cu current collector was composed of 80% Bi nanowires, 10% carbon black, and 10% PVDF as the binder. The electrolyte was 1 M $LiPF_6$ in EC/EMC, and the counter electrode was Li metal foil separated from the Bi electrode by a CELGARD 2325 membrane.

Synchrotron Characterization. *In situ* synchrotron XRD was done at the Advanced Photon Source (beamline 11-ID-C, energy ~ 110 keV, $\Delta d/d \sim 0.01$) at Argonne National Laboratory. Prior to the test, the coin cell was customized by drilling a central hole through both the cathode and anode caps for X-ray penetration and noise signal reduction. Capton tapes were used to tightly seal the coin cell to prevent electrolyte leakage. A galvanostatic mode was used in the battery cycling with a constant current value of 40 mA/g.

DFT Calculations of Li Interaction into Bi. DFT calculations[32] were performed using the Vienna *Ab Initio* Simulations Package (VASP) code[33] employing the generalized-gradient approximation using the Perdew, Burke, and Ernzerhof[34] functional to account for the exchange–correlation effects. For systems with an even number of electrons, nonspin-polarized calculations are performed, and for systems with an odd number of electrons, unrestricted spin-polarized calculations are performed. Lithium migration paths and barriers are determined using the linear nudged-elastic-band method as implemented in VASP code. For all calculations, a cutoff energy of 400 eV is used. A further increase of cutoff energy to 450 eV led to the change of the total energy of <0.01 eV. All structural optimizations are carried out until the forces, acting on atoms, are below 0.01 eV/Å. The criteria for energy change is set to 0.1 eV. For the bulk Bi phase, we use a $3 \times 3 \times 2$ supercell created based on a Bi hexagonal unit cell with 6 atoms (lattice constant $a = b = 13.14$ Å, and $c = 22.99$ Å), allowing all atoms to relax while holding the lattice parameters and volume of the supercell fixed. In the case of the vacuum cell, a vacuum layer of 15 Å is used to prevent the interactions between the periodic structures in the direction perpendicular to the surface. For the vacuum cell, we use the $2 \times 3 \times 1$ k-point mesh.[35] We have also checked the size of the vacuum layer over the surface to ensure no interaction between the slabs. Additionally, in order to ensure that the slab thickness is chosen properly and represents the properties of the macroscopic crystal structure, the Li binding energy was calculated for two different slab thicknesses. The Li binding energy increased by 2%, comparing the slabs with 7 against the slab with 9 layers.

ASSOCIATED CONTENT

Supporting Information

The Supporting Information is available free of charge at https://pubs.acs.org/doi/10.1021/acsnano.0c06597.

Movie S1: Full Li–Bi alloying process of the single Bi nanowire (MP4)

Figure S1, additional STEM images and simulated SAED patterns of Bi nanowires; Figures S2–S4, possible Li–Bi configuration based on simulation results; and Figure S5, the voltage profiles upon cycling (PDF)

AUTHOR INFORMATION

Corresponding Authors

Vitaliy Yurkiv – *Department of Mechanical and Industrial Engineering, University of Illinois at Chicago, Chicago, Illinois 60607, United States;* orcid.org/0000-0002-3407-891X; Email: vyurkiv@uic.edu

Reza Shahbazian-Yassar – *Department of Mechanical and Industrial Engineering, University of Illinois at Chicago, Chicago, Illinois 60607, United States;* orcid.org/0000-0002-7744-4780; Email: rsyassar@uic.edu

Jun Lu – *Chemical Sciences and Engineering Division, Argonne National Laboratory, Lemont, Illinois 60439, United States;* orcid.org/0000-0003-0858-8577; Email: junlu@anl.gov

Authors

Yifei Yuan – *Chemical Sciences and Engineering Division, Argonne National Laboratory, Lemont, Illinois 60439, United States; Department of Mechanical and Industrial Engineering, University of Illinois at Chicago, Chicago, Illinois 60607, United States*

Wentao Yao – *Department of Mechanical and Industrial Engineering, University of Illinois at Chicago, Chicago, Illinois 60607, United States;* orcid.org/0000-0003-1653-769X

Tongchao Liu – *Chemical Sciences and Engineering Division, Argonne National Laboratory, Lemont, Illinois 60439, United States*

Boao Song – *Department of Mechanical and Industrial Engineering, University of Illinois at Chicago, Chicago, Illinois 60607, United States;* orcid.org/0000-0003-3124-3235

Farzad Mashayek – *Department of Mechanical and Industrial Engineering, University of Illinois at Chicago, Chicago, Illinois 60607, United States;* orcid.org/0000-0003-1187-4937

Complete contact information is available at: https://pubs.acs.org/10.1021/acsnano.0c06597

Author Contributions

[§]Y.Y. and W.Y. contributed equally to this work. W.Y. synthesized Bi nanowires. Y.Y. carried out the electrochemical tests and TEM analyses and wrote the manuscript under the direction of J.L. and R.S.-Y. Y.Y. and T.L. designed and analyzed the synchrotron XRD experiment/results. V.Y. and F.M. carried out the DFT calculations and took part in discussions, analyses, and writing of the manuscript. B.S. contributed to figure design and discussion.

Notes

The authors declare no competing financial interest.

ACKNOWLEDGMENTS

Work at Argonne National Laboratory was supported by the U.S. Department of Energy (DOE), Office of Energy Efficiency and Renewable Energy, Vehicle Technologies Office. Argonne

National Laboratory is operated for DOE Office of Science by UChicago Argonne, LLC, under contract number DE-AC02-06CH11357. Use of the Advanced Photon Source (APS) {beamline 11-ID-C}, Office of Science user facility, was supported by the U.S. Department of Energy, Office of Science, Office of Basic Energy Sciences, under contract no. DE-AC02-06CH11357. V.Y. and R. S.-Y. efforts were supported by NSF CBET award no. 1805938. This work made use of instruments in the Electron Microscopy Service (Research Resources Center, UIC). Y.Y. acknowledges funding from the Argonne National Laboratory-University of Illinois at Chicago subcontract (no. 4J-30361). The present DFT calculations were supported by the National Science Foundation Extreme Science and Engineering Discovery Environment (XSEDE) award no. TG-DMR180106.

REFERENCES

(1) Ji, L.; Lin, Z.; Alcoutlabi, M.; Zhang, X. Recent Developments in Nanostructured Anode Materials for Rechargeable Lithium-Ion Batteries. *Energy Environ. Sci.* **2011**, *4*, 2682−2699.

(2) Yuan, Y.; Amine, K.; Lu, J.; Shahbazian-Yassar, R. Understanding Materials Challenges for Rechargeable Ion Batteries with *in Situ* Transmission Electron Microscopy. *Nat. Commun.* **2017**, *8*, 15806.

(3) Nitta, N.; Wu, F.; Lee, J. T.; Yushin, G. Li-Ion Battery Materials: Present and Future. *Mater. Today* **2015**, *18*, 252−264.

(4) Lan, J. L.; Jin, Y.; Qin, C.; Yu, Y.; Yang, X. Bio-Inspired Rose-Like Bi@Nitrogen-Enriched Carbon towards High-Performance Lithium-Ion Batteries. *ChemistrySelect* **2017**, *2*, 7178−7184.

(5) Zhang, Y.; Wang, Q.; Wang, B.; Mei, Y.; Lian, P. N-Doped Graphene/Bi Nanocomposite with Excellent Electrochemical Properties for Lithium−Ion Batteries. *Ionics* **2017**, *23*, 1407−1415.

(6) Park, C.-M.; Yoon, S.; Lee, S.-I.; Sohn, H.-J. Enhanced Electrochemical Properties of Nanostructured Bismuth-Based Composites for Rechargeable Lithium Batteries. *J. Power Sources* **2009**, *186*, 206−210.

(7) Yin, H.; Li, Q.; Cao, M.; Zhang, W.; Zhao, H.; Li, C.; Huo, K.; Zhu, M. Nanosized-Bismuth-Embedded 1D Carbon Nanofibers as High-Performance Anodes for Lithium-Ion and Sodium-Ion Batteries. *Nano Res.* **2017**, *10*, 2156−2167.

(8) Zhao, Y.; Manthiram, A. High-Capacity, High-Rate Bi−Sb Alloy Anodes for Lithium-Ion and Sodium-Ion Batteries. *Chem. Mater.* **2015**, *27*, 3096−3101.

(9) Hong, W.; Wang, A.; Li, L.; Qiu, T.; Li, J.; Jiang, Y.; Zou, G.; Peng, H.; Hou, H.; Ji, X. Bi Dots Confined by Functional Carbon as High-Performance Anode for Lithium Ion Batteries. *Adv. Funct. Mater.* **2020**, 2000756.

(10) Dai, R.; Wang, Y.; Da, P.; Wu, H.; Xu, M.; Zheng, G. Indirect Growth of Mesoporous Bi@C Core−Shell Nanowires for Enhanced Lithium-Ion Storage. *Nanoscale* **2014**, *6*, 13236−13241.

(11) Huang, J.; Lin, X.; Tan, H.; Zhang, B. Bismuth Microparticles as Advanced Anodes for Potassium-Ion Battery. *Adv. Energy Mater.* **2018**, *8*, 1703496.

(12) Su, D.; Dou, S.; Wang, G. Bismuth: A New Anode for the Na-Ion Battery. *Nano Energy* **2015**, *12*, 88−95.

(13) Sottmann, J.; Herrmann, M.; Vajeeston, P.; Hu, Y.; Ruud, A.; Drathen, C.; Emerich, H.; Fjellvåg, H.; Wragg, D. S. How Crystallite Size Controls the Reaction Path in Nonaqueous Metal Ion Batteries: The Example of Sodium Bismuth Alloying. *Chem. Mater.* **2016**, *28*, 2750−2756.

(14) Ellis, L.; Wilkes, B.; Hatchard, T.; Obrovac, M. *in Situ* XRD Study of Silicon, Lead and Bismuth Negative Electrodes in Nonaqueous Sodium Cells. *J. Electrochem. Soc.* **2014**, *161*, A416−A421.

(15) Xue, P.; Wang, N.; Fang, Z.; Lu, Z.; Xu, X.; Wang, L.; Du, Y.; Ren, X.; Bai, Z.; Dou, S.; et al. Rayleigh-Instability-Induced Bismuth Nanorod@Nitrogen-Doped Carbon Nanotubes as a Long Cycling and High Rate Anode for Sodium-Ion Batteries. *Nano Lett.* **2019**, *19*, 1998−2004.

(16) Guidotti, R. A.; Masset, P. J. Thermally Activated ("Thermal") Battery Technology: Part IV. Anode Materials. *J. Power Sources* **2008**, *183*, 388−398.

(17) Janish, M. T.; Mackay, D. T.; Liu, Y.; Jungjohann, K. L.; Carter, C. B.; Norton, M. G. TEM *in Situ* Lithiation of Tin Nanoneedles For Battery Applications. *J. Mater. Sci.* **2016**, *51*, 589−602.

(18) Liu, X. H.; Zheng, H.; Zhong, L.; Huang, S.; Karki, K.; Zhang, L. Q.; Liu, Y.; Kushima, A.; Liang, W. T.; Wang, J. W.; et al. Anisotropic Swelling and Fracture of Silicon Nanowires During Lithiation. *Nano Lett.* **2011**, *11*, 3312−3318.

(19) Liu, X. H.; Wang, J. W.; Huang, S.; Fan, F.; Huang, X.; Liu, Y.; Krylyuk, S.; Yoo, J.; Dayeh, S. A.; Davydov, A. V.; et al. *in Situ* Atomic-Scale Imaging of Electrochemical Lithiation in Silicon. *Nat. Nanotechnol.* **2012**, *7*, 749.

(20) Liang, W.; Yang, H.; Fan, F.; Liu, Y.; Liu, X. H.; Huang, J. Y.; Zhu, T.; Zhang, S. Tough Germanium Nanoparticles under Electrochemical Cycling. *ACS Nano* **2013**, *7*, 3427−3433.

(21) Zhao, K.; Wang, W. L.; Gregoire, J.; Pharr, M.; Suo, Z.; Vlassak, J. J.; Kaxiras, E. Lithium-Assisted Plastic Deformation of Silicon Electrodes in Lithium-Ion Batteries: A First-Principles Theoretical Study. *Nano Lett.* **2011**, *11*, 2962−2967.

(22) Kaghazchi, P. Mechanism of Li Intercalation into Si. *Appl. Phys. Lett.* **2013**, *102*, No. 093901.

(23) McDowell, M. T.; Lee, S. W.; Nix, W. D.; Cui, Y. 25th Anniversary Article: Understanding the Lithiation of Silicon and Other Alloying Anodes for Lithium-Ion Batteries. *Adv. Mater.* **2013**, *25*, 4966−4985.

(24) Gan, Z.; Gu, M.; Tang, J.; Wang, C.-Y.; He, Y.; Wang, K. L.; Wang, C.; Smith, D. J.; McCartney, M. R. Direct Mapping of Charge Distribution During Lithiation of Ge Nanowires Using Off-Axis Electron Holography. *Nano Lett.* **2016**, *16*, 3748−3753.

(25) Li, Q.; Liu, H.; Yao, Z.; Cheng, J.; Li, T.; Li, Y.; Wolverton, C.; Wu, J.; Dravid, V. P. Electrochemistry of Selenium with Sodium and Lithium: Kinetics and Reaction Mechanism. *ACS Nano* **2016**, *10*, 8788−8795.

(26) Andrews, A. M.; Romanov, A.; Speck, J.; Bobeth, M.; Pompe, W. Development of Cross-Hatch Morphology during Growth of Lattice Mismatched Layers. *Appl. Phys. Lett.* **2000**, *77*, 3740−3742.

(27) Sobiech, M.; Wohlschlögel, M.; Welzel, U.; Mittemeijer, E.; Hügel, W.; Seekamp, A.; Liu, W.; Ice, G. E. Local, Submicron, Strain Gradients as the Cause of Sn Whisker Growth. *Appl. Phys. Lett.* **2009**, *94*, 221901.

(28) Li, J.; Yang, F.; Ye, J.; Cheng, Y.-T. Whisker Formation on a Thin Film Tin Lithium-Ion Battery Anode. *J. Power Sources* **2011**, *196*, 1474−1477.

(29) Zhang, L. Q.; Liu, X. H.; Perng, Y.-C.; Cho, J.; Chang, J. P.; Mao, S. X.; Ye, Z. Z.; Huang, J. Y. Direct Observation of Sn Crystal Growth During the Lithiation and Delithiation Processes of SnO_2 Nanowires. *Micron* **2012**, *43*, 1127−1133.

(30) Wang, C.; Wang, L.; Li, F.; Cheng, F.; Chen, J. Bulk Bismuth as a High-Capacity and Ultralong Cycle-Life Anode for Sodium-Ion Batteries by Coupling with Glyme-Based Electrolytes. *Adv. Mater.* **2017**, *29*, 1702212.

(31) Xiong, P.; Bai, P.; Li, A.; Li, B.; Cheng, M.; Chen, Y.; Huang, S.; Jiang, Q.; Bu, X.-H.; Xu, Y. Xu, Y. Bismuth Nanoparticle@Carbon Composite Anodes for Ultralong Cycle Life and High-Rate Sodium-Ion Batteries. *Adv. Mater.* **2019**, *31*, 1904771.

(32) Kohn, W.; Sham, L. J. Self-Consistent Equations Including Exchange And Correlation Effects. *Phys. Rev.* **1965**, *140*, A1133.

(33) Kresse, G.; Furthmüller, J. Efficient Iterative Schemes for *ab Initio* Total-Energy Calculations Using a Plane-Wave Basis Set. *Phys. Rev. B: Condens. Matter Mater. Phys.* **1996**, *54*, 11169.

(34) Perdew, J. P.; Burke, K.; Ernzerhof, M. Generalized Gradient Approximation Made Simple. *Phys. Rev. Lett.* **1996**, *77*, 3865.

(35) Monkhorst, H. J.; Pack, J. D. Special Points for Brillouin-Zone Integrations. *Phys. Rev. B* **1976**, *13*, 5188.

https://dx.doi.org/10.1021/acsnano.0c06597
ACS Nano 2020, 14, 15669−15677